

Na₂KSb/Cs_xSb interface engineering for high-efficiency photocathodes

S.A. Rozhkov^{1,2,*} V.V. Bakin¹ V.S. Rusetsky^{1,3} D.A. Kustov¹ V.A. Golyashov^{1,2,4}
A.Yu. Demin³ H.E. Scheibler^{1,2} V.L. Alperovich^{1,2} and O.E. Tereshchenko^{1,2,4,†}

¹*Rzhanov Institute of Semiconductor Physics, Siberian Branch, Russian Academy of Sciences,
Novosibirsk 630090, Russia*

²*Novosibirsk State University, Novosibirsk 630090, Russia*

³*CJSC “EKTRAN FEP”, Novosibirsk 630060, Russia*

⁴*Synchrotron Radiation Facility SKIF, Boreskov Institute of Catalysis, Siberian Branch,
Russian Academy of Sciences, Koltsovo 630559, Russia*

 (Received 9 April 2024; revised 19 June 2024; accepted 25 June 2024; published 2 August 2024)

Optical and photoemission measurements were performed on alkali antimonide Na₂KSb and Na₂KSb/Cs_xSb photocathodes in order to determine their energy-band diagrams, elucidate the photoemission pathways, and explore the options for interface engineering in order to reach high quantum efficiencies of the photocathodes. This study is motivated by the recent discovery of optical orientation in Na₂KSb and emission of spin-polarized electrons from Na₂KSb/Cs_xSb photocathodes [V.S. Rusetsky *et al.*, Phys. Rev. Lett. **129**, 166802 (2022)]. We have shown that the band gap E_g of Na₂KSb at $T = 295$ K lies within the range of 1.40–1.44 eV. The Na₂KSb surface activation by the deposition of Cs and Sb results in effective electron affinity decrease by approximately 0.37 eV, and in an increase of the quantum efficiency up to 0.2 electrons per incident photon. The analysis of longitudinal energy distribution curves (EDCs) proves that the surface of activated Na₂KSb/Cs_xSb photocathodes have negative effective electron affinity of approximately -0.1 and -0.25 eV at $T = 295$ and 80 K, respectively. EDC measurements under increasing photon energy $\hbar\omega$ demonstrate the transition of photoemission pathway from the surface states’ photoionization at $\hbar\omega < E_g$ to the emission from the conduction-band bottom at $\hbar\omega \approx E_g$ and from the states with high kinetic energy in the conduction band at $\hbar\omega > E_g$. EDCs measured at 80 K reveal a highly directional photoelectron emission from the Na₂KSb/Cs_xSb photocathode, as compared to the p -GaAs(Cs,O) photocathode. This fact, along with the observed significant, by an order of magnitude, increase in the photoluminescence intensity under the Na₂KSb surface activation by Cs and Sb, indicates relatively weak diffuse scattering in the “quasiepitaxial” Cs_xSb activation layer of a Na₂KSb/Cs_xSb photocathode, compared to strong scattering in the amorphous (Cs,O) activation layer of a p -GaAs(Cs,O) photocathode.

DOI: [10.1103/PhysRevApplied.22.024008](https://doi.org/10.1103/PhysRevApplied.22.024008)

I. INTRODUCTION

Photocathodes based on the emission of photoelectrons from solids into vacuum are widely used in various devices—photomultipliers, image intensifiers, and spin-polarized electron sources. Polarized electron sources are key instruments for the development of modern and future electron-ion [1–3] and electron-positron colliders [4–6]. Also, polarized electron sources are used in various analytical methods, such as spin-polarized transmission electron microscopy and spin-polarized low-energy electron microscopy [7,8]. All these applications require robust, low-emittance, and efficient spin-polarized sources.

At present, the highest quantum efficiencies (QEs) are obtained for semiconductor photocathodes based on p -GaAs and other III-V compounds with negative effective electron affinity (NEA), at which the vacuum level E_{vac} lies below the conduction-band bottom in the bulk of a semiconductor E_c [9]. The state of NEA is achieved by the deposition of cesium and oxygen, which form an activation layer of subnanometer thickness. In the NEA state, the photoemission threshold of the photocathode is decreased from several electron volts at the clean semiconductor surface down to the semiconductor band gap E_g , and the QE is increased by several orders of magnitude, up to approximately 0.5 electrons per incident photon [10,11]. Due to the effect of optical orientation of electron spins under the excitation by circularly polarized light [12], semiconductor photocathodes make it possible to produce beams of spin-polarized electrons [13,14]. The

*Contact author: rozhkovs@isp.nsc.ru

†Contact author: teresh@isp.nsc.ru

maximum spin polarization of electrons emitted from unstrained GaAs photocathodes is $P = 50\%$. Lifting the valence-band degeneracy in strained photocathodes or superlattices allows increasing this value up to $P \approx 90\%$ [15]. The record parameters of semiconductor photocathodes are based on their crystalline perfection and detailed knowledge of the electronic band structure, mechanisms of photoexcitation, transport, and escape of photoelectrons into vacuum.

Another group of photocathodes, which are also widely used in photoemission devices, is based on alkali antimonide compounds [16–18]. The most effective in this group are multialkali $\text{Na}_2\text{KSb}/\text{Cs}_x\text{Sb}$ photocathodes (MPs). An MP consists of a 100–140-nm-thick polycrystalline Na_2KSb active layer deposited on a glass substrate and covered with a thin (approximately 1 nm) “activation” layer of cesium and antimony in order to reduce the work function ϕ [19]. In MPs, QE near the photoemission threshold reaches approximately 0.1 electrons per incident photon [19,20]. These values are significantly lower than for NEA photocathodes based on III-V semiconductor compounds. However, MPs have a number of advantages, in particular, fabrication simplicity and higher stability of photoemission properties. It was shown in Refs. [21–23] that alkali antimonide photocathodes are capable of stable electron-beam generation with record high-average currents, along with acceptable values of QE, response time, and mean transverse energy (MTE) of emitted electrons.

In the recent work by Rusetsky *et al.* [24], the effect of optical orientation of photoelectron spins during the excitation by circularly polarized light has been demonstrated in $\text{Na}_2\text{KSb}/\text{Cs}_x\text{Sb}$ photocathodes, as well as a high spin

polarization of the emitted photoelectrons. These results open wide prospects for developing stable high-brightness spin-polarized electron sources based on MPs for accelerator facilities and analytical instrumentation. As in the case of III-V NEA photocathodes [14,25], the realization of these prospects also requires detailed knowledge of the electronic band structure of the active layer, the energy diagram of the photocathode–vacuum interface and the mechanisms of photoelectron emission into vacuum.

At present, the data on the electronic band structure and photoemission properties of multialkali $\text{Na}_2\text{KSb}/\text{Cs}_x\text{Sb}$ photocathodes available in the literature are contradictory. The first uncertainty is related to the band gap E_g of the Na_2KSb active layer: the values of E_g given in the literature vary from 1.0 eV [17,18,22,26] to 1.4 eV [27,28]. The second unresolved question is whether the effective electron affinity χ^* on the surface of activated $\text{Na}_2\text{KSb}/\text{Cs}_x\text{Sb}$ photocathode is positive or negative. The energy-band diagrams of photocathodes with positive effective electron affinity (PEA) and NEA are shown in Figs. 1(a) and 1(b), respectively. In a large number of papers [17,18,22,26,27,29,30], the effective affinity of $\text{Na}_2\text{KSb}/\text{Cs}_x\text{Sb}$ photocathode at room temperature was considered to be positive $\chi^* \approx 0.3$ eV, while in Ref. [28] it was found that it is negative $\chi^* \approx -0.1$ eV.

Along with the questions about the band gap and effective affinity at room temperature, photoemission properties of MPs at low temperatures, which so far were studied insufficiently, are of scientific and practical interest. This interest is due to the temperature dependence of the spin-relaxation rate of photoelectrons in semiconductors [31,32], which can significantly affect the spin polarization of electrons emitted from the MPs. In addition,

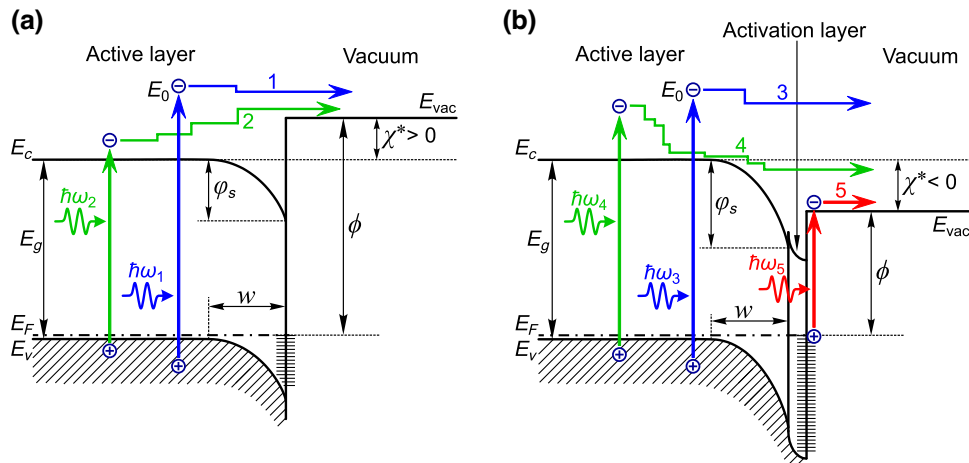


FIG. 1. Energy-band diagrams of photocathodes with PEA ($\chi^* > 0$) (a) and NEA ($\chi^* < 0$) (b). Relevant photoemission pathways are shown: direct emission of hot photoelectrons (1, 3), emission of thermalized photoelectrons (2, 4) and photoemission from occupied surface states (5). E_c and E_v are the conduction-band bottom and the valence-band top in the bulk of the active layer, respectively, E_F is the Fermi level, E_{vac} is the vacuum level, E_0 is the initial energy of photoexcited electrons, ϕ is the work function, ϕ_s is the surface band bending, and w is the width of the band-bending region.

cooling of the semiconductor photocathode can reveal new photoemission pathways [33–35] and enable a decrease in the MTE of emitted photoelectrons [36,37].

To resolve the contradictions and fill the gaps in the literature, in this work, we studied the optical and photoemission properties of Na₂KSb/Cs_xSb photocathodes, which demonstrate the effects of optical orientation and emission of spin-polarized photoelectrons [24,38]. The spectra of QE, light absorption, and photoluminescence of these photocathodes, as well as energy distributions of photoelectrons emitted into vacuum were measured in the temperature range 80–295 K. It was established that the state of NEA is characteristic of the Na₂KSb/Cs_xSb photocathodes both at low and room temperatures. It was shown that, at low temperatures, the angular distribution of photoelectrons emitted into vacuum is concentrated near the normal to the photocathode surface.

II. EXPERIMENTAL DETAILS

Planar vacuum photodiodes [20,24,33,35,39] with semi-transparent Na₂KSb and Na₂KSb/Cs_xSb photocathodes were fabricated for these studies. The photocathode growth was carried out in an ultrahigh vacuum chamber with the base pressure of 10^{−8} Pa by a simultaneous deposition of Na, K, and Sb on a flat glass window until the required thickness of the Na₂KSb active layer was reached [19].

Photoemission current was monitored at all stages of photocathode preparation. The glass substrate temperature during the active layer growth was approximately 470 K [18,19]. The Na₂KSb photocathode activation was carried out by depositing Cs and Sb at $T \approx 420$ K [18] until the maximal photocurrent was obtained. This procedure results in a luminous sensitivity up to 850 $\mu\text{A}/\text{lm}$ at $T = 295$ K. The measured spectra of optical transmission and reflection of the fabricated photocathodes were similar to those published in Refs. [19,28]. The thickness of the Na₂KSb active layers was about 120 nm and was determined from the interference observed in the reflectance spectra. The vacuum photodiode was formed by mounting the photocathode and anode parallel to each other at a distance of about 0.5 mm in an alumina ceramic body. Anodes were made by depositing Cr layers or by bonding the Al_{0.11}Ga_{0.89}As layer to flat glass substrates [24]. The working diameter of the photodiodes was equal to 20 mm. The schematic representation of a vacuum photodiode and its photograph are shown in Figs. 2(a) and 2(b), respectively. A typical quantum efficiency spectrum and the QE map of the Na₂KSb/Cs_xSb photocathode are shown in Figs. 2(c) and 2(d), respectively. QE values up to 0.2 were obtained with relative variations over the working area less than 10%. To compare Na₂KSb/Cs_xSb and *p*-GaAs(Cs,O) photocathodes, we fabricated planar vacuum photodiodes with *p*-GaAs(Cs,O) photocathodes [35].

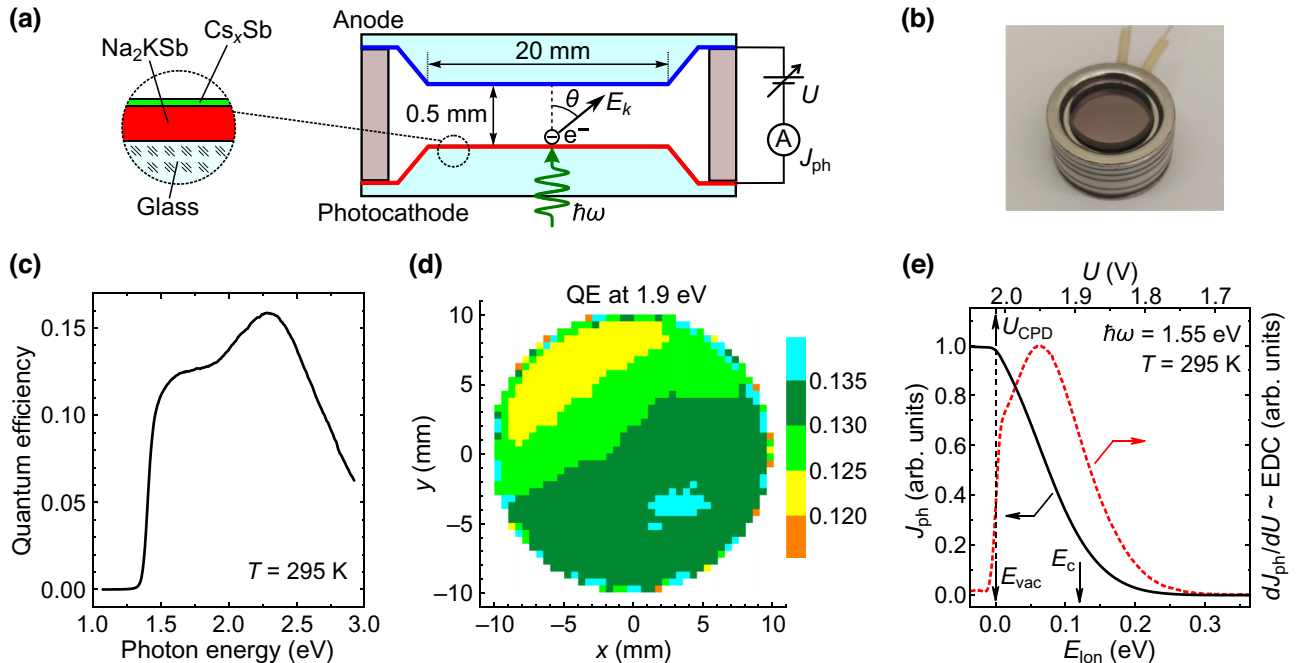


FIG. 2. Structure of a photodiode with a Na₂KSb/Cs_xSb photocathode and its photoemission properties measured at 295 K. (a) Schematic cross section of the vacuum photodiode. (b) Photograph of the photodiode. (c) Quantum efficiency spectrum. (d) Quantum efficiency map measured at $\hbar\omega = 1.9$ eV. (e) Photocurrent-voltage curve $J_{\text{ph}}(U)$ (solid line) and its derivative (dash-dot line) measured at $\hbar\omega = 1.55$ eV. The longitudinal component of the electron kinetic energy E_{lon} is plotted along the lower axis. The contact potential difference U_{CPD} , vacuum level E_{vac} , and the conduction-band minimum in the bulk of Na₂KSb E_c are shown with arrows.

All the data presented in this work were obtained on vacuum photodiodes. The measurements of reflectance $R(\hbar\omega)$, transmittance $T(\hbar\omega)$, photoluminescence $I_{\text{PL}}(\hbar\omega)$, and photoemission quantum efficiency $\text{QE}(\hbar\omega)$ spectra of the photocathodes, as well as the longitudinal energy distribution curves (EDC) of photoelectrons emitted into vacuum, were carried out in the temperature range 80–295 K. The measurements of $R(\hbar\omega)$ and $T(\hbar\omega)$ spectra were done on a special photodiode with an anode replaced by a transparent glass window. The $R(\hbar\omega)$ and $T(\hbar\omega)$ spectra were measured at an incidence angle of approximately equal to 20° . The absorbance spectrum $A(\hbar\omega)$ of the photocathode was calculated from the following relation:

$$T(\hbar\omega) + R(\hbar\omega) + A(\hbar\omega) = 1. \quad (1)$$

EDC measurements were performed in the planar vacuum photodiodes, which were used as electron spectrometers with a uniform retarding electric field [33,35]. In such a spectrometer, photoelectrons reach the anode if the longitudinal component of their kinetic energy E_{lon} satisfies the condition:

$$E_{\text{lon}} > e(U_{\text{CPD}} - U), \quad (2)$$

where $E_{\text{lon}} = E_k \cos^2(\theta)$, E_k and θ are the total kinetic energy of the photoelectron and the polar emission angle [see Fig. 2(a)], respectively, U_{CPD} is the contact potential difference between the photocathode and the anode, U is the acceleration voltage, e is the electron charge modulus. The electron energy distribution $N_e(E_{\text{lon}})$ is proportional to the derivative of the photoemission current J_{ph} with respect to U [33,35]:

$$N_e(E_{\text{lon}}) \sim dJ_{\text{ph}}(U)/dU. \quad (3)$$

A typical photocurrent-voltage curve $J_{\text{ph}}(U)$ of a photodiode with $\text{Na}_2\text{KSb}/\text{Cs}_x\text{Sb}$ photocathode and its derivative are shown in Fig. 2(e). The value of contact potential difference U_{CPD} and, accordingly, the position of E_{vac} were determined by the position of the extremum in the second derivative of the $J_{\text{ph}}(U)$ curve and are marked with arrows in Fig. 2(e).

The vacuum photodiode was mounted in a continuous-flow nitrogen optical cryostat. The photocathode was illuminated in the transmission mode by a light spot of approximately 1 mm in diameter. A halogen lamp and a monochromator were used as a light source with a calibrated photon flux. To measure EDC, the sum of a dc voltage U and a small ac sinusoidal voltage U_{\sim} of about 10 meV in amplitude was applied to the photodiode. Then, the ac component of the photocurrent, which is proportional to the derivative of $J_{\text{ph}}(U)$, was measured by the lock-in amplifier. The electron spectrometer resolution was determined both by the value of U_{\sim} and by the nonuniformities of the anode work function within the light spot area.

III. RESULTS

A. Photoemission and optical spectra of Na_2KSb and $\text{Na}_2\text{KSb}/\text{Cs}_x\text{Sb}$ photocathodes at 295 K

To determine the energy-band diagrams and to elucidate the photoemission pathways, we compared the photoemission properties of Na_2KSb and $\text{Na}_2\text{KSb}/\text{Cs}_x\text{Sb}$ photocathodes. For this purpose, two photocathodes with identical Na_2KSb layers were simultaneously fabricated in a growth chamber. Then one of the photocathodes was immediately sealed in a vacuum photodiode. The second photocathode was sealed after activation of its surface with Cs and Sb. The photoemission quantum efficiency spectra $\text{QE}(\hbar\omega)$ measured at 295 K at these Na_2KSb and $\text{Na}_2\text{KSb}/\text{Cs}_x\text{Sb}$ photocathodes are shown in Fig. 3(a). The measurements of the spectra were done at acceleration voltage $U = 10$ V. As can be seen, the QE spectrum of the Na_2KSb photocathode contains two thresholds at $\hbar\omega = 1.435 \pm 0.01$ eV

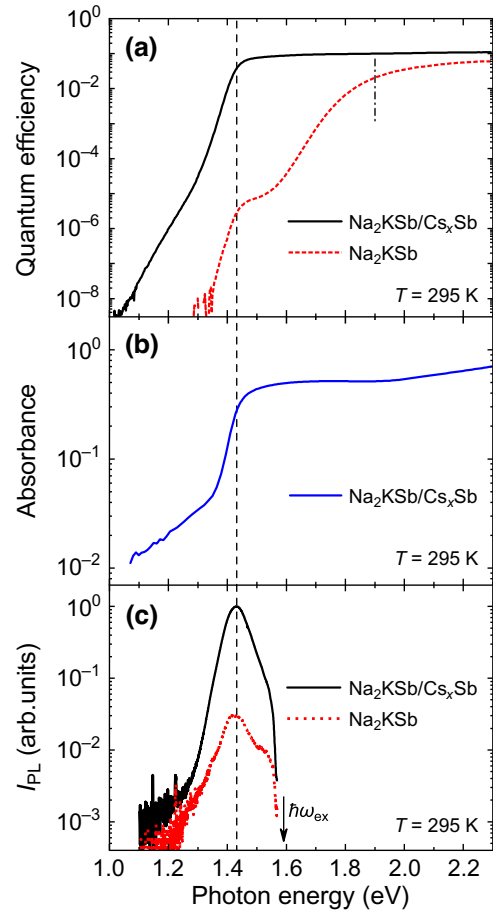


FIG. 3. Photoemission and optical spectra of Na_2KSb and $\text{Na}_2\text{KSb}/\text{Cs}_x\text{Sb}$ photocathodes at 295 K. (a) Quantum efficiency spectra $\text{QE}(\hbar\omega)$. The vertical dash-dot line indicates the threshold of direct photoemission at 1.9 eV. The vertical dashed line indicates the threshold at band gap $E_g = 1.43$ eV. (b) Absorbance spectrum $A(\hbar\omega)$. (c) Photoluminescence spectra $I_{\text{PL}}(\hbar\omega)$. Excitation energy $\hbar\omega_{\text{ex}} = 1.59$ eV is shown with an arrow.

and $\hbar\omega = 1.90 \pm 0.04$ eV. The threshold energies were determined by the peak positions in the QE($\hbar\omega$) derivative [40] and are marked by vertical lines. The high-energy threshold corresponds to the direct emission of hot photoelectrons into vacuum [pathway 1 in Fig. 1(a)]. The low-energy threshold is due to the photon-enhanced thermionic emission (PETE) [41,42], i.e., emission of thermalized photoelectrons that are excited in the Na₂KSb conduction band with initial energies lower than E_{vac} and receive the energy necessary for emission from the crystal lattice by the absorption of phonons [pathway 2 in Fig. 1(a)]. The position of the high-energy threshold is determined by the PEA value of Na₂KSb photocathode χ^* , and the position of the low-energy threshold coincides with the Na₂KSb layer band gap E_g . It is seen in Fig. 3(a) that the QE($\hbar\omega$) spectrum of the Na₂KSb/Cs_xSb photocathode has only one threshold located at $\hbar\omega = 1.43 \pm 0.01$ eV. The coincidence in the positions (within approximately 5 meV) and shapes of the low-energy threshold in the QE($\hbar\omega$) spectra of the two photocathodes fabricated in the same growth process and different only in the presence or absence of a approximately 1-nm-thick activation layer indicates that this is the threshold of interband transitions, and the band gap in the Na₂KSb layer $E_g = 1.43 \pm 0.01$ eV at room temperature. In the QE spectrum of the Na₂KSb/Cs_xSb photocathode, we do not observe the high-energy threshold, which is associated with the direct emission of hot photoelectrons in the state with PEA. This means that the deposition of the activation layer reduced the effective affinity χ^* by approximately 0.5 eV, down to negative or near-zero values. In such a photocathode, at $\hbar\omega > E_g$, a fraction of photoelectrons escape into vacuum without significant energy loss [pathway 3 in Fig. 1(b)] [25,43]. The remaining photoelectrons thermalize to the conduction-band bottom in the Na₂KSb layer bulk, reach the band-bending region and may undergo energy and momentum scattering at the surface before escaping into vacuum [pathway 4 in Fig. 1(b)] [25,33]. At $\hbar\omega < E_g$, the QE spectrum of the Na₂KSb/Cs_xSb photocathode consists of two exponential regions. The high-energy exponential region with a slope of approximately equal to 15 meV is due to the interband transitions between the tails of the density of states of the valence and conduction bands of the Na₂KSb layer [44]. The low-energy exponential region with a slope of approximately equal to 28 meV is due, presumably, to the emission of electrons into vacuum from the occupied surface states [pathway 5 in Fig. 1(b)] and defect states in the band-bending region [45–47].

Shown in Fig. 3(b) is the absorbance spectrum $A(\hbar\omega)$ of Na₂KSb/Cs_xSb photocathode measured at 295 K on a special photodiode with a transparent glass window instead of an anode. It is seen that the low-energy part of the spectrum contains two exponential regions with different slopes. In the steep region, the absorbance increases by an order of magnitude with increasing $\hbar\omega$ in the range

of 1.35–1.45 eV. This region is due to the onset of interband optical transitions in the Na₂KSb layer. The band-gap value determined from the position of the maximum in the $A(\hbar\omega)$ derivative was $E_g = 1.42 \pm 0.01$ eV. The thresholds coincidence in the QE($\hbar\omega$) spectra of Na₂KSb and Na₂KSb/Cs_xSb photocathodes with the threshold position in the $A(\hbar\omega)$ spectrum of Na₂KSb/Cs_xSb photocathode, with the accuracy of 10 meV, further confirms that the low-energy thresholds in the QE($\hbar\omega$) spectra are due to the onset of interband transitions in the Na₂KSb layers. The less steep exponential tail in the $A(\hbar\omega)$ spectrum at $\hbar\omega < 1.35$ eV is presumably caused by electronic transitions involving defect states or by variations in the band gap due to fluctuations in the chemical composition of the active layer [27,48,49]. The weak variations in $A(\hbar\omega)$ at $\hbar\omega > E_g$ are due to the light interference in the Na₂KSb layer [19,27].

The photoluminescence spectra $I_{\text{PL}}(\hbar\omega)$ of the same Na₂KSb and Na₂KSb/Cs_xSb photocathodes are shown in Fig. 3(c). The spectra were measured at 295 K for excitation energy $\hbar\omega_{\text{ex}} = 1.59$ eV. The maxima of the $I_{\text{PL}}(\hbar\omega)$ spectra of Na₂KSb and Na₂KSb/Cs_xSb photocathodes are at $\hbar\omega = 1.425 \pm 0.005$ eV and $\hbar\omega = 1.430 \pm 0.005$ eV, respectively, and coincide with the position of the low-energy thresholds in the QE spectra with the accuracy of approximately 5 meV. This indicates that the $I_{\text{PL}}(\hbar\omega)$ spectra correspond to the interband transitions in the Na₂KSb layer. The integral photoluminescence intensity of the Na₂KSb/Cs_xSb photocathode is by an order of magnitude higher than that of the Na₂KSb photocathode. This, probably, indicates that the Cs_xSb activation layer passivates the nonradiative recombination centers at the emitting surface. The sharp drop in I_{PL} at $\hbar\omega > 1.55$ eV is due to the use of an optical filter to cut off the excitation laser radiation. Small differences in the shape and width of the spectra are due to the parasitic contribution of the photoluminescence signal from the photocathode glass window [24]. Thus, the analysis of QE($\hbar\omega$), $A(\hbar\omega)$, and $I_{\text{PL}}(\hbar\omega)$ spectra presented in Fig. 3 proves that, at 295 K, the Na₂KSb active layer band gap for these particular MPs lies in the range of $E_g = 1.42$ – 1.43 eV, and the effective electron affinity of the Na₂KSb/Cs_xSb photocathodes is close to zero or negative.

B. Photoelectrons energy distributions of Na₂KSb and Na₂KSb/Cs_xSb photocathodes at 295 K

In order to determine the energy-band diagrams of the MPs, the longitudinal energy-distribution curves of emitted electrons were measured. The EDCs of Na₂KSb/Cs_xSb and Na₂KSb photocathodes are shown in Figs. 4(a) and 4(b), respectively. The EDCs are measured at $T = 295$ K at various $\hbar\omega$; the longitudinal energy is referred to E_c . The EDCs are normalized so that the area under each EDC is equal to the QE value at the respective photon

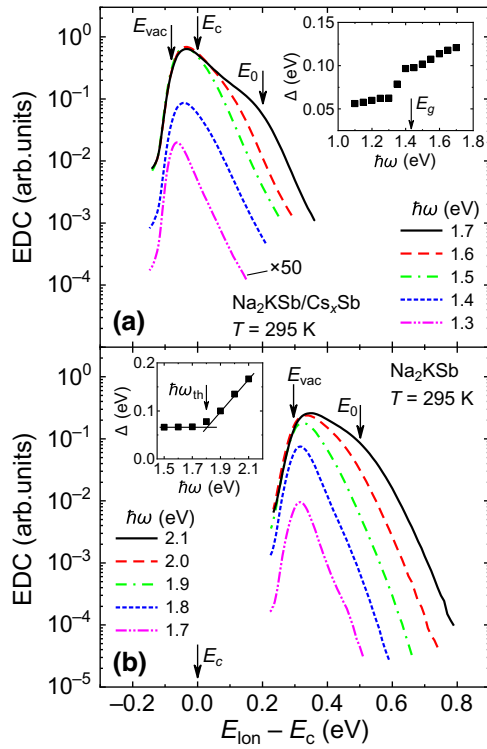


FIG. 4. Evolution of EDCs with varying $\hbar\omega$ at 295 K for (a) the $\text{Na}_2\text{KSb}/\text{Cs}_x\text{Sb}$ photocathode and (b) the Na_2KSb photocathode. The areas under EDCs are normalized to QE values. Vacuum level E_{vac} , the conduction-band minima in the bulk of Na_2KSb E_c and initial energies of excited photoelectrons E_0 are marked with arrows. Insets: the EDC width (FWHM) dependences on photon energy Δ on the photon energy $\hbar\omega$. Na_2KSb band gap E_g and direct photoemission threshold $\hbar\omega_{\text{th}}$ are marked with arrows.

energy $\hbar\omega$. The procedure for determining the energy position of E_c is described below and illustrated in Fig. 5. It can be seen that, for all $\hbar\omega$, the EDCs of both photocathodes are asymmetric peaks with the low-energy edge corresponding to the vacuum level E_{vac} . The insets of Figs. 4(a) and 4(b) show the dependences of the distributions FWHM Δ on the photon energy.

As can be seen in the inset in Fig. 4(a), at $\hbar\omega < 1.3$ eV, when the photoemission occurs from the surface states [pathway 5 in Fig. 1(b)], the width of the EDC of the activated $\text{Na}_2\text{KSb}/\text{Cs}_x\text{Sb}$ photocathode is approximately 60 meV and increases slowly with increasing $\hbar\omega$. At $\hbar\omega \approx 1.35$ eV, the sharp increase in the EDC width up to approximately equal to 100 meV is observed. This increase is due to the onset of the interband optical transitions in the Na_2KSb layer. At $\hbar\omega \geq E_g$ the emission of electrons generated in the Na_2KSb layer bulk dominates over the photoemission from the surface states. In the range $\hbar\omega = 1.4$ – 1.5 eV, the shape of the energy distributions weakly depends on $\hbar\omega$, and their high-energy tail has an approximately exponential shape with a slope of

approximately equal to 38 meV. This indicates the emission into vacuum of thermalized photoelectrons from the conduction-band bottom in the Na_2KSb layer bulk [pathway 4 in Fig. 1(b)] [43]. With further increase in $\hbar\omega$, the EDC width increases due to the increase in the contribution of hot photoelectrons, which undergo only a partial energy relaxation before their emission into vacuum [pathway 3 in Fig. 1(b)] [25,43]. Also, at sufficiently high photon energies $\hbar\omega > 1.6$ eV, a distinct shoulder emerges in the high-energy region of the EDC, which shifts to higher energies with increasing $\hbar\omega$. In Fig. 4(a) we marked the position of this shoulder E_0 for the distribution measured at $\hbar\omega = 1.7$ eV. The positions of the shoulders can be determined with the accuracy of 20 meV from the positions of the high-energy minima in the EDC derivatives shown in Fig. 5. The main minima in the derivatives, which are observed at lower energies, are related to the emission of electrons thermalized to the conduction-band bottom in the Na_2KSb layer bulk. The positions of the low-energy maxima of the EDC derivatives correspond to vacuum-level energy E_{vac} . As can be seen in the inset of Fig. 5, the position of the high-energy minimum depends linearly on $\hbar\omega$. This result is consistent with the linear dependence of the initial energy of photoexcited electrons in the conduction band E_0 on $\hbar\omega$ [25]:

$$E_0(\hbar\omega) = E_c + (\hbar\omega - E_g)/(1 + m_e/m_h), \quad (4)$$

where m_e and m_h are effective masses of electrons and holes, respectively.

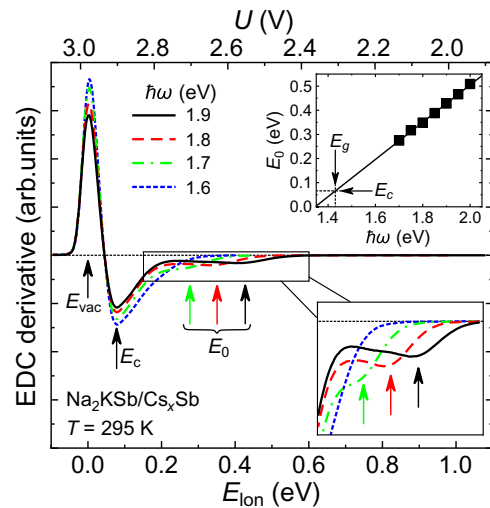


FIG. 5. Evolution of EDC derivatives with varying $\hbar\omega$ at 295 K for $\text{Na}_2\text{KSb}/\text{Cs}_x\text{Sb}$ photocathode. Vacuum level E_{vac} , the conduction-band minimum in the bulk of Na_2KSb E_c and initial energies of excited photoelectrons E_0 are marked with arrows. Inset: the dependence $E_0(\hbar\omega)$. The band gap E_g and E_c are marked with arrows.

Thus, the high-energy shoulder of the energy distributions is related to the emission into vacuum of photoelectrons that have not undergone scattering in the Na₂KSb layer [25]. The measured slope of the $E_0(\hbar\omega)$ dependence is equal to 0.80 ± 0.05 . The ratio of the effective masses of electrons and holes in Na₂KSb estimated from the slope is equal to $m_e/m_h \approx 0.25$. A detailed analysis of the EDCs high-energy features of the Na₂KSb/Cs_xSb photocathodes, which provides the data on the electronic band structure of the photocathode active layer [25], is beyond the scope of this work and will be presented elsewhere. In accordance with expression (4), the extrapolation of the dependence $E_0(\hbar\omega)$ down to $\hbar\omega = E_g$, as shown in the inset of Fig. 5, allows us to determine the position of E_c relative to E_{vac} , and, correspondently, the sign and magnitude of the affinity χ^* . As is seen in Fig. 5, the E_c position lies at higher energies than E_{vac} . Thus, the effective affinity of activated Na₂KSb/Cs_xSb photocathode is negative. For this particular Na₂KSb/Cs_xSb photocathode at room temperature, the effective affinity $\chi^* = -0.08 \pm 0.02$ eV.

It turned out that the value of E_c , determined as shown in the inset of Fig. 5, coincides with the accuracy of 20 meV with the position of the main minimum in the EDC derivatives measured at $\hbar\omega > E_g$. In the following, the values of E_c for NEA photocathodes were determined by the position of this minimum, as shown in Fig. 5.

The EDCs measured at various $\hbar\omega$ at the nonactivated Na₂KSb photocathode are shown in Fig. 4(b). At $\hbar\omega < 1.7$ eV, the shape of the EDCs is independent of $\hbar\omega$, with a distribution width of approximately 66 meV. This indicates the generation of photoelectrons in the conduction band of Na₂KSb with initial energies E_0 below the E_{vac} . For the emission into vacuum, photoelectrons must receive additional energy from the lattice by the absorption of phonons [pathway 2 in Fig. 1(a)]; therefore, only a small fraction of photoelectrons escapes into vacuum [42]. The EDC's width $\Delta \approx 66$ meV is close to that of the Na₂KSb/Cs_xSb photocathodes at $\hbar\omega < E_g$ and significantly exceeds thermal energy $kT \approx 25$ meV, presumably, due to relatively high nonuniformities of the Cr anode work functions of these two photodiodes. At $\hbar\omega > 1.7$ eV the EDC width starts to increase with increasing $\hbar\omega$ due to the direct emission of hot photoelectrons, when $E_0 > E_{vac}$ [25] [pathway 1 in Fig. 1(a)]. At energies close to E_0 , as for the activated Na₂KSb/Cs_xSb photocathode, a characteristic shoulder appears in the measured EDC; the shoulder shifts to higher energies with increasing $\hbar\omega$. In Fig. 4(b), the position of the high-energy shoulder is marked for the EDC measured at $\hbar\omega = 2.1$ eV. As seen in Fig. 4(b), for all photon energies, the high-energy tail of EDCs of the nonactivated Na₂KSb photocathode has an approximately exponential shape with a slope of approximately equal to 33 meV.

It should be noted that, due the state of PEA, the high-energy shoulders in the EDCs of nonactivated Na₂KSb

photocathode are observed at higher $\hbar\omega$, compared to those observed for the Na₂KSb/Cs_xSb NEA photocathode. It turned out that, upon the increase in $\hbar\omega$, these shoulders are significantly broadened, so it is difficult to obtain the dependence $E_0(\hbar\omega)$ with an accuracy sufficient for determining E_c . Therefore, we used two alternative methods to determine E_c and χ^* of the Na₂KSb photocathode. The first method is based on the assumption that the intersection point of the two linear regions on the $\Delta(\hbar\omega)$ dependence, shown in the inset of Fig. 4(b), corresponds to the direct photoemission threshold $\hbar\omega_{th} = 1.80 \pm 0.04$ eV at which $E_0(\hbar\omega_{th}) = E_c + \chi^*$. To find the value of χ^* , it is also reasonable to assume that the slope of the $E_0(\hbar\omega)$ dependence is the same for both Na₂KSb and Na₂KSb/Cs_xSb photocathodes since they have identical Na₂KSb active layers. Using relation (4), we determined the position of E_c and the value of PEA of the Na₂KSb photocathode $\chi^* = 0.30 \pm 0.05$ eV.

The second method is based on the comparison of the EDCs of Na₂KSb and Na₂KSb/Cs_xSb photocathodes measured at $\hbar\omega > \hbar\omega_{th}$. In this case, photoelectrons have equal initial energies E_0 , form identical energy distributions in the bulk of the Na₂KSb layers and, therefore, may produce high-energy tails of similar shape in the EDCs. The result of comparison of the EDCs, which are normalized by the QE value, is shown in Fig. 6. In order to align the position and amplitude of the high-energy regions of the distributions, the EDC of Na₂KSb photocathode is shifted by 0.37 eV towards higher energies and multiplied by a factor of 0.25. As is seen in Fig. 6, the high-energy regions of the EDCs coincide over a wide range of

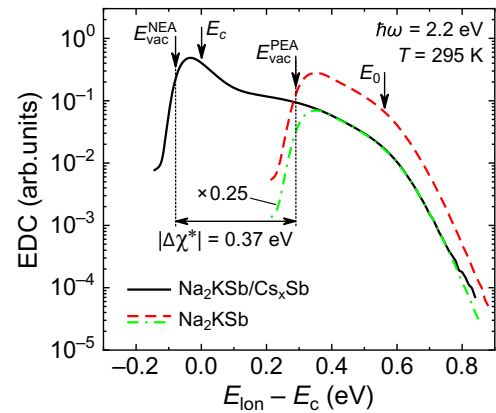


FIG. 6. EDCs of Na₂KSb/Cs_xSb (solid line) and Na₂KSb (dashed line) photocathodes measured at $\hbar\omega = 2.2$ eV. $T = 295$ K. The areas under EDCs are normalized to QE values. For comparison, the EDC of Na₂KSb was multiplied by a factor of 0.25 (dash-dot line). The vacuum-level positions of Na₂KSb/Cs_xSb and Na₂KSb photocathodes E_{vac}^{NEA} and E_{vac}^{PEA} , respectively, the conduction-band minimum in the bulk of Na₂KSb E_c and initial energy of excited photoelectrons E_0 are marked with arrows.

energies. Consequently, the Na_2KSb photocathode activation by the deposition of Cs_xSb layer leads to a decrease in the E_{vac} position relative to E_c by $\Delta\chi^* = -0.37 \pm 0.02$ eV and to a decrease in the amplitude of the high-energy region of the EDC by a factor of approximately 4. Taking the value $\chi^* = -0.08 \pm 0.02$ eV for the $\text{Na}_2\text{KSb}/\text{Cs}_x\text{Sb}$ photocathode, we conclude that the PEA of Na_2KSb photocathode equals $\chi^* = 0.29 \pm 0.04$ eV. Thus, the values of χ^* for the nonactivated Na_2KSb photocathode obtained by two different methods coincide within the experimental accuracy.

C. Photoemission spectra of $\text{Na}_2\text{KSb}/\text{Cs}_x\text{Sb}$ photocathodes in the temperature range 80–295 K

To elucidate the photoelectron emission mechanisms and to determine the energy-band diagrams of MPs at low temperatures, the $\text{QE}(\hbar\omega)$ spectra of $\text{Na}_2\text{KSb}/\text{Cs}_x\text{Sb}$ photocathode were measured at various temperatures in the range of 80–295 K and are shown in Fig. 7. The positions of $\text{QE}(\hbar\omega)$ thresholds at different temperatures are marked with arrows in Fig. 7.

It is seen that, with the decreasing temperature, the photoemission threshold shifts toward higher photon energies, in accordance with increasing the band gap. Consider the temperature evolution of low-energy region $\hbar\omega < E_g$ of QE spectra (Fig. 7). It is seen that the decrease in temperature from 295 to 80 K does not essentially change the shape of the exponential tail associated with the threshold of interband transitions in the Na_2KSb layer. In contrast, upon cooling, the shape of the spectra at lower $\hbar\omega$ undergoes a significant modification: structureless exponential tail, with a slope of approximately equal to 28 meV at 295 K, is gradually transformed into a broad shoulder. At

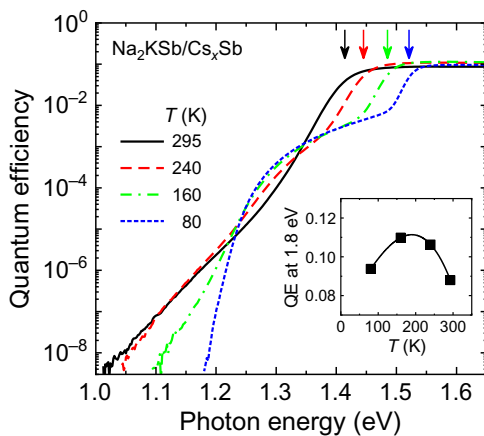


FIG. 7. Quantum efficiency spectra of $\text{Na}_2\text{KSb}/\text{Cs}_x\text{Sb}$ photocathode at various temperatures. The band-gap energies are marked with arrows. Inset: temperature dependence of the quantum efficiency at $\hbar\omega = 1.8$ eV. The line is drawn to guide the eye.

$T = 80$ K the low-energy exponential tail of this shoulder has a slope of approximately equal to 8 meV. The closeness of the exponential slopes to the thermal energy kT confirms the assumption that these tails are due to the emission of electrons from filled surface states [46,50].

As seen in the inset of Fig. 7, for $\hbar\omega > E_g$, upon cooling from 295 to 80 K, the quantum efficiency of the transmission-mode $\text{Na}_2\text{KSb}/\text{Cs}_x\text{Sb}$ photocathode first increases, reaches its maximum value at about 160 K and then decreases. Similar nonmonotonic behavior was observed on NEA GaAs photocathodes [25]. The increase in QE with decreasing T is explained by the increase in the modulus of NEA $|\chi^*| = E_c - E_{\text{vac}}$. The QE decrease at lower temperatures is presumably related to the decrease in the diffusion length of photoelectrons.

The temperature dependences of the $\text{QE}(\hbar\omega)$ thresholds and $I_{\text{PL}}(\hbar\omega)$ maxima, which represent the band-gap values, are shown in Fig. 8 for a set of typical $\text{Na}_2\text{KSb}/\text{Cs}_x\text{Sb}$ photocathodes. The photoluminescence maxima positions of “modern” MPs studied in Ref. [28] and the temperature dependence of the band gap in intrinsic GaAs [51] are also shown in Fig. 8 for comparison. It is seen that all dependences are similar; the overall variations of the band-gap values in the studied photocathodes are within approximately 40 meV. The band-gap variations from sample to sample are, presumably, due to small variations in the stoichiometry of the samples. There is also a systematic shift, up to 20 meV toward lower energies, of the $I_{\text{PL}}(\hbar\omega)$ maxima with respect to the $\text{QE}(\hbar\omega)$ thresholds. Such a low-energy shift of the $I_{\text{PL}}(\hbar\omega)$ maxima in doped semiconductors can be explained by the recombination between the conduction band and impurity states, which contribute to the formation of the near-band-gap photoluminescence [52].

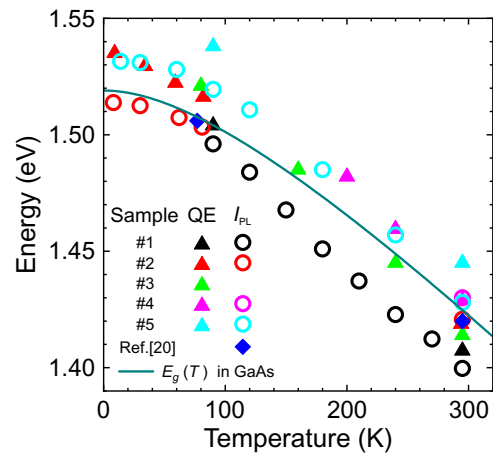


FIG. 8. Positions of $\text{QE}(\hbar\omega)$ thresholds (triangles) and $I_{\text{PL}}(\hbar\omega)$ maxima (circles) for several $\text{Na}_2\text{KSb}/\text{Cs}_x\text{Sb}$ photocathodes (samples #1–5) at various temperatures. The temperature dependence of GaAs band gap is shown by the solid line.

D. Photoelectron energy distributions of Na₂KSb/Cs_xSb photocathodes at 80 K

The EDCs of the Na₂KSb/Cs_xSb NEA photocathode were measured at 80 K for various $\hbar\omega$ and are shown in Fig. 9. The dependence of the EDCs full widths at the half-maximum on the photon energy $\Delta(\hbar\omega)$ is shown in the inset of Fig. 9. Cooling to $T = 80$ K reduced thermal broadening and led to a decrease in the E_{vac} position relative to E_c , which resulted in a significant increase in the NEA modulus. For this particular Na₂KSb/Cs_xSb photocathode, at $T = 80$ K, the effective affinity $\chi^* = -0.27 \pm 0.02$ eV. The photocathode cooling allowed us to trace more clearly, compared to room temperature, the transition of the emission pathways upon the increase in $\hbar\omega$ from the region $\hbar\omega < E_g$, where the photoemission from surface states dominates [pathway 5 in Fig. 1(b)], to the region $\hbar\omega > E_g$, where photoelectrons excited by interband optical transitions in the Na₂KSb active layer yield the major contribution to photoemission [pathways 3 and 4 in Fig. 1(b)].

At $T = 80$ K and $\hbar\omega < 1.25$ eV, the EDC shape is almost independent of $\hbar\omega$, with a width of approximately 29 meV. It is reasonable to assume that the photon energy in this spectral region does not exceed work function ϕ , and photoemission occurs from the partially filled surface states above the Fermi level [46]. This assumption is consistent with the low-energy shape of the QE($\hbar\omega$) spectrum at 80 K (see Fig. 7). In contrast, at $\hbar\omega > 1.25$ eV, an increase in $\hbar\omega$ leads to a linear growth of Δ with a slope close to 1. Therefore, the high-energy edge of the EDCs is determined by the emission of photoelectrons excited from the Fermi level [47,50]. We determined the work function of the Na₂KSb/Cs_xSb photocathode at 80 K

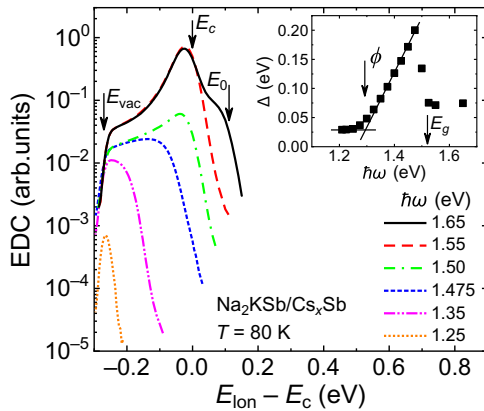


FIG. 9. Evolution of EDCs with varying $\hbar\omega$ at 80 K for Na₂KSb/Cs_xSb photocathode. The areas under EDCs are normalized to QE values. Vacuum level E_{vac} , the conduction-band minimum in the bulk of Na₂KSb E_c and initial energy of excited photoelectrons E_0 are marked with arrows. Inset: the dependence of the EDC width (FWHM) on photon energy $\Delta(\hbar\omega)$. Na₂KSb bandgap E_g and work function ϕ are marked with arrows.

$\phi = 1.29 \pm 0.05$ eV as the intersection point of the two linear regions on the $\Delta(\hbar\omega)$ dependence, as shown in the inset of Fig. 9.

When the photon energy reaches the threshold of interband transitions $E_g(80 \text{ K}) = 1.52 \pm 0.01$ eV, a narrow peak emerges at E_c on the broad distribution of photoelectrons emitted from surface states (see Fig. 9). This peak is associated with the emission of thermalized photoelectrons from the conduction-band bottom of the Na₂KSb layer [pathway 4 in Fig. 1(b)]. Unlike room temperature, at $T = 80$ K, as can be seen in the inset of Fig. 9, the onset of interband transitions is accompanied by an abrupt drop in the EDC width from $\Delta \approx 200$ meV to $\Delta \approx 75$ meV, which is equal to the width of the thermalized photoelectrons peak. At $\hbar\omega = 1.55$ eV, the high-energy tail of the EDC has an approximately exponential shape with a slope of approximately 14 meV at $T = 80$ K. Upon further increase in $\hbar\omega$, a shoulder emerges in the high-energy region of the EDC due to the emission of hot and ballistic photoelectrons from the Na₂KSb layer bulk [pathway 3 in Fig. 1(b)]. The comparison of Figs. 9 and 4(a) shows that, at low temperature, the shoulder is revealed much more distinctly due to the reduced thermal broadening.

IV. DISCUSSION

The measurements and analysis of optical and photoemission spectra, as well as energy distributions of emitted photoelectrons, allowed us to determine the parameters of the energy-band diagram of multialkali Na₂KSb/Cs_xSb photocathode. The results are summarized in Fig. 10.

At 295 K the band gap E_g of the Na₂KSb layer of the investigated photocathodes lies in the range of 1.40–1.44 eV. These values coincide with the accuracy of 0.1 eV with those obtained in Refs. [27,28] and exceed the E_g values given in Refs. [17,26] by 0.3–0.4 eV. One of

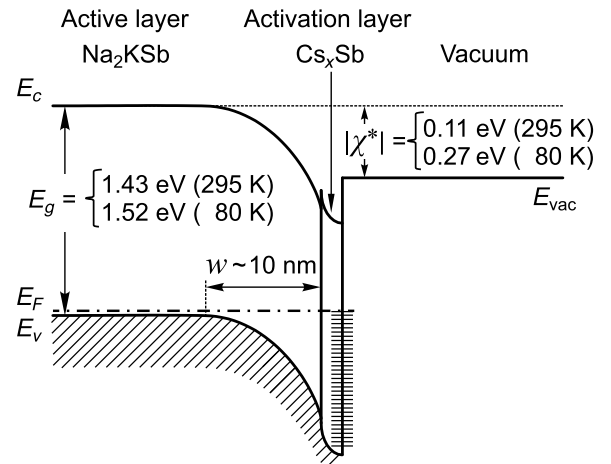


FIG. 10. The energy-band diagram of a typical multialkali Na₂KSb/Cs_xSb photocathode.

the possible reasons for the discrepancy in the E_g values may be differences in the chemical composition of multialkali photocathodes studied by different authors. Indeed, as was shown by the density-functional-theory (DFT) calculations [53], the band gaps of cubic Na_2KSb and hexagonal NaK_2Sb are close to 1.5 and 1.0 eV, respectively. However, this explanation contradicts the previous studies, which showed that the chemical composition of the active layer of high-efficient MPs is close to Na_2KSb [16,29,48,49]. The fact that the cubic Na_2KSb demonstrates superior photoemission properties, compared to hexagonal NaK_2Sb , is probably related to the n -type doping of the latter. According to Refs. [16,17,29,49], the alkali antimonide compounds with a hexagonal structure are n -type semiconductors, which usually have upward band bending at the surface and, therefore, increased work function.

The analysis of the phase diagram of the Na-K-Sb system, which was studied in Ref. [54], further proves that the variations in the active-layer composition cannot explain the discrepancy in the E_g values. Indeed, it was shown in Ref. [54] that this system forms cubic solid solution $\text{Na}_{2-x}\text{K}_{1+x}\text{Sb}$ in the range of $x = 0\text{--}0.05$. According to the estimates based on the available data on ternary III-V semiconductor compounds [51], variations in the composition of $\text{Na}_{2-x}\text{K}_{1+x}\text{Sb}$ phase within this range should lead to variations in E_g less than 0.1 eV. Beyond this range the formation of NaK_2Sb or Na_3Sb hexagonal crystallites occurs with the band gaps of 0.8–1.1 eV [17,27,53,55]. A substantial fraction of these crystallites would lead to an additional absorption threshold around 1.0 eV. The weak optical absorption below 1.4 eV observed in Ref. [28] and in the present study [see Fig. 3(b)] indicates that high-efficiency MPs contain only a small fraction (approximately 1%) of the hexagonal phase.

Following the approach used in Refs. [27,28], we measured the QE and absorbance spectra of relatively thick (100–150 nm) Na_2KSb and $\text{Na}_2\text{KSb}/\text{Cs}_x\text{Sb}$ films, with distinct sharp thresholds of interband transitions at $\hbar\omega \approx 1.4$ eV. In contrast, in the work by Spicer [17], due to the small thickness of the studied films, it was difficult to determine E_g from the absorbance spectra; so, E_g was determined by the threshold in the photoconductivity spectrum. In Ref. [26], the band gap of Na_2KSb and $\text{Na}_2\text{KSb}/\text{Cs}_x\text{Sb}$ photocathodes was also determined from the photoconductivity spectra, while the absorbance spectra were not measured. We believe that the analysis of the absorbance spectra is a more reliable and direct method to determine E_g , because, along with the interband transitions, optical transitions involving impurities and defects could make a significant contribution to the photoconductivity spectra of thin polycrystalline films [27,56,57]. Upon cooling, the Na_2KSb layer band gap E_g of the investigated photocathodes increases to 1.51–1.54 eV at 80 K.

The results of the present study prove that a non-activated Na_2KSb photocathode has a positive effective

affinity $\chi^* \approx 0.3$ eV. Upon the Na_2KSb surface activation by depositing Cs and Sb, a transition from PEA to NEA occurs. The obtained change in the effective electron affinity due to the activation equals $\Delta\chi^* = -0.37 \pm 0.02$ eV. Thus, in the investigated $\text{Na}_2\text{KSb}/\text{Cs}_x\text{Sb}$ photocathodes, the effective affinity χ^* is negative and lies in the range from -0.08 to -0.13 eV at room temperature. This fact well agrees with Ref. [28] and contradicts many other papers [17,18,26,58], where the effective affinity χ^* of the $\text{Na}_2\text{KSb}/\text{Cs}_x\text{Sb}$ photocathode was considered to be positive, with the value of χ^* in the range of 0.3–0.55 eV. Broad variations in the values of χ^* can be explained by differences in empirical photocathode activation techniques. Indeed, as was shown recently, the stoichiometry of Cs-Sb compound strongly depends on the substrate temperature [59]; this dependence can lead to variations in the effective electron affinity. We believe, however, that the variations in the sign and magnitude of χ^* are mostly due to the use of underestimated values of E_g in the calculation of χ^* . Indeed, in Refs. [17,18,26,58] it was assumed that $E_g \approx 1.0$ eV, and this yielded positive effective affinity $\chi^* \approx 0.3$ eV. However, if we assume that $E_g \approx 1.4$ eV, then the value of χ^* decreases by 0.4 eV and becomes negative, in agreement with Ref. [28] and the results of the present work. It should be noted that Hoene [27] obtained the band-gap value in the range of 1.3–1.4 eV and still slightly positive affinity $\chi^* = 0\text{--}0.05$ eV, probably, due to the peculiarities of the photocathode growth and activation procedures. Upon cooling to 80 K, the effective electron affinity χ^* of investigated $\text{Na}_2\text{KSb}/\text{Cs}_x\text{Sb}$ photocathodes further decreases and lies in the range from -0.25 to -0.30 eV.

It should be noted that the values of the surface band bending φ_s and the width of the band-bending region w (see Figs. 1 and 10) in the Na_2KSb layer are not directly derived from our experimental data; these values are also not available in the literature. The NEA state of the $\text{Na}_2\text{KSb}/\text{Cs}_x\text{Sb}$ photocathode unambiguously proves that the Na_2KSb layer is p -doped and the band bending is downwards, as for the NEA photocathodes based on p -doped III-V semiconductors. For a reasonable estimate we can assume that, similar to p -GaAs, the Fermi level on the Na_2KSb surface is pinned near the middle of the bandgap; so, $\varphi_s \sim 0.7$ eV [26,60,61]. The concentration of acceptors N_a , which is needed to calculate w , can be estimated from the position of the Fermi level E_F with respect to the top of the valence band E_v , which, in its turn, can be determined from the obtained values of the band gap E_g , effective electron affinity χ^* and work function ϕ :

$$(E_F - E_v) = E_g + \chi^* - \phi. \quad (5)$$

According to formula (5), at 80 K the Fermi level in the Na_2KSb layer bulk is located near the top of valence band $E_F \approx E_v \pm 0.05$ eV, in agreement with the previous

studies [26,28,30,60]. Taking $E_F = E_v$, we estimate $N_a \gtrsim 10^{19} \text{ cm}^{-3}$. This yields the estimate for the band-bending region width $w \lesssim 10 \text{ nm}$.

The obtained results indicate the similarity of the multialkali Na₂KSb/Cs_xSb and III-V semiconductor *p*-GaAs(Cs,O) photocathodes [24,28]. Indeed, the photocathode band gaps have close values at room and low temperatures. The activation of both types of photocathodes leads to the state of NEA. However, along with these similarities, in this work we found fundamental differences in the optical and photoemission properties of Na₂KSb/Cs_xSb and *p*-GaAs(Cs,O) photocathodes, which indicate, in our opinion, significant differences in the activation-layer properties of these photocathodes.

The first difference clearly shows up in the shape of low-temperature EDCs. The EDCs of the *p*-GaAs(Cs,O) and Na₂KSb/Cs_xSb photocathodes measured in the transmission mode at $T = 80 \text{ K}$ are shown in Fig. 11. For comparison, the distributions are normalized to the maximum. For both photocathodes, the photon energies $\hbar\omega > E_g$ were chosen so that the majority of photoelectrons are thermalized to the conduction-band bottom in the active-layer bulk before emission.

As can be seen in Fig. 11, the photoelectrons emitted from *p*-GaAs(Cs,O) are approximately uniformly distributed over the entire energy range from the vacuum level to E_c . A narrow high-energy peak located near E_c is formed by a small fraction of “ballistic” photoelectrons emitted into the vacuum without energy and momentum scattering at the surface and move predominantly along the normal to the surface [33,34]. In contrast, the major fraction of

photoelectrons undergoes momentum and energy scattering at the surface and forms a broad longitudinal energy distribution. As it was shown earlier [62], a significant part of emitted electrons moves in vacuum almost parallel to the GaAs surface with the total kinetic energy close to $E_c - E_{\text{vac}}^{\text{GaAs}}$; this indicates a strong elastic diffuse scattering of photoelectrons at the *p*-GaAs(Cs,O) surface.

In contrast to *p*-GaAs(Cs,O), EDC of the Na₂KSb/Cs_xSb photocathode consists of a strong peak located near E_c and a weak low-energy wing extending down to the vacuum level $E_{\text{vac}}^{\text{MP}}$. The comparison shows that, in the EDC of Na₂KSb/Cs_xSb, the fraction of photoelectrons emitted into vacuum with low E_{lon} is by an order of magnitude smaller than that in *p*-GaAs(Cs,O). Consequently, the momentum scattering of photoelectrons at the Na₂KSb/Cs_xSb photocathode surface is much weaker, compared to the *p*-GaAs(Cs,O), and the velocity vectors of emitted photoelectrons are concentrated near the normal to the emitting surface. The observation of highly directional photoemission from polycrystalline Na₂KSb/Cs_xSb photocathodes, in contrast to the photoemission in a broad solid angle from high-quality monocrystalline *p*-GaAs(Cs,O) photocathodes, is an unexpected, interesting and potentially useful fact. The exact reason for this fact is not clear. Presumably, in the *p*-GaAs(Cs,O) photocathode, photoelectrons undergo diffuse scattering in the amorphous (Cs,O) activation layer [63–67]. Strong diffuse scattering at the (Cs,O) activation layer and its amorphousness are proved by the observed disappearance of diffraction spots and a strong increase of the diffuse background in the low-energy electron diffraction images under the GaAs activation [65]. The amorphous nature of the (Cs,O) activation layer stems from the lattice mismatch and nonisomorphism between a monocrystalline GaAs substrate and Cs-O compounds [68], along with relatively low temperatures (approximately equal to 300 K) of cesium and oxygen deposition. In contrast, the Na₂KSb surface activation by Cs and Sb occurs at elevated temperatures, which usually facilitate the growth of ordered layers [18,19,69]. Also, the activation layer of MP can be isomorphous to the Na₂KSb active layer [18,19,48,49]. Finally, the lattice-matching restrictions for the ordered growth can be weakened in the case of a polycrystalline MP with a crystallite size of approximately 100 nm [69]. Indeed, according to Ref. [70], the critical thickness of the ordered pseudomorphic epitaxial layer significantly increases with decreasing the lateral dimensions of the substrate to the nm scale. The formation of such a “quasiepitaxial” Cs_xSb activation layer with an ordered structure on each crystallite of the Na₂KSb active layer can explain relatively weak diffuse scattering of photoelectrons at the Na₂KSb/Cs_xSb photocathode surface. One can assume that the Cs₃Sb activation layer is grown on top of the Na₂KSb active layer [22]. However, previous studies indicate that the activation layer of high-efficiency MPs may have various chemical compositions due to

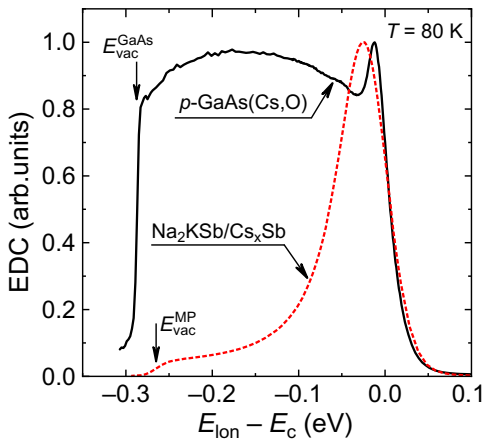


FIG. 11. EDCs of the transmission-mode photocathodes at $T = 80 \text{ K}$: *p*-GaAs(Cs,O) (solid line) and Na₂KSb/Cs_xSb (dashed line). Excitation energies $\hbar\omega_{\text{ex}}$ for *p*-GaAs(Cs,O) and Na₂KSb/Cs_xSb photocathodes were 1.85 and 1.55 eV, respectively. The curves are normalized to maximum values. The vacuum-level positions of photocathodes $E_{\text{vac}}^{\text{GaAs}}$ and $E_{\text{vac}}^{\text{MP}}$ are marked with arrows.

the peculiarities of activation procedure, such as possible incorporation of Na and K atoms into the activation layer due to the diffusion from the bulk or unintentional deposition from the growth chamber [18,19,48,49]. It is desirable to validate the directional emission from MPs by the measurements of the transverse momentum distribution of the emitted photoelectrons [71]. The preparations for these measurements are under way. The results will be presented in a separate publication.

The second difference is that the Na₂KSb photocathode activation by Cs and Sb increases the photoluminescence intensity I_{PL} by an order of magnitude [see Fig. 3(c)], while the activation-induced changes in I_{PL} of the p -GaAs(Cs,O) photocathode do not exceed approximately 20% [72,73]. The increase in I_{PL} upon activation may indicate the passivation of nonradiative recombination centers on the emitting surface. Another explanation consists in the decrease of the effective surface recombination velocity in a heavily doped p -type semiconductor due to an increase in the specular reflection coefficient of electrons on the surface [74,75]. This second hypothesis is consistent with the shape of the EDCs measured at low temperature and, again, indicates the weakness of photoelectron diffuse scattering at the surface of Na₂KSb/Cs_xSb photocathodes with a quasicrystalline Cs_xSb activation layer. The increase in reflection is also consistent with the several-fold decrease in the amplitude of the high-energy region of EDC (see Fig. 6).

A problem with the above hypothesis is that to explain activation-induced increase in I_{PL} by an order of magnitude, one should assume that the rates of nonradiative recombination in the Na₂KSb layer bulk and at its interface with glass are, at least, an order of magnitude smaller than on the emitting surface. This assumption is inconsistent with the general conception about high concentration of nonradiative recombination centers in a polycrystalline Na₂KSb film. In its turn, the conception is in agreement with the experimental value of photoelectron diffusion length $L_D \approx 110$ nm [28], approximately equal to the Na₂KSb film thickness.

The nonradiative recombination rate at the glass-Na₂KSb interface should also be high. It is known that, in transmission-mode p -GaAs(Cs,O) photocathodes, the reduction of the nonradiative recombination rate at the interface with glass is due to the use of a high-quality lattice-matched GaAs/(Al,Ga)As heterojunction [9,76]. The suppression of nonradiative recombination in the bulk and at the glass interface of MPs can be explained by the existence of quasidelectric fields due to the chemical composition gradient or electric fields due to the doping gradient in the Na₂KSb layer bulk. These fields accelerate photoelectrons toward the emitting surface so that photoelectrons can reach the emitting surface without undergoing nonradiative recombination in the bulk or at the interface with glass.

An alternative explanation of the activation-induced increase in I_{PL} by an order of magnitude consists in the activation-induced modification of Na₂KSb layer bulk properties. It is known that, upon activation by Cs and Sb, the electrical conductivity of the Na₂KSb film can increase by an order of magnitude [29]. This increase can be associated with an increase in the hole concentration in the Na₂KSb layer, and, therefore, lead to an increase in the radiative recombination rate and I_{PL} magnitude [76,77]. In addition, possible diffusion of Cs and Sb along grain boundaries may lead to the passivation of nonradiative recombination centers in the Na₂KSb layer bulk and at the glass-Na₂KSb interface. Thus, the question about the reasons for the I_{PL} increase during the activation of Na₂KSb/Cs_xSb photocathode remains open and requires further studies.

Thus, the results obtained in this work allow us to get deeper understanding of the factors that determine the photoemission properties of polycrystalline multialkali Na₂KSb/Cs_xSb photocathodes, as well as the reasons for the similarities and differences between the MPs and single-crystal p -GaAs(Cs,O) photocathodes. The first similarity is the closeness of the band-gap values in Na₂KSb and GaAs. Second, a state of NEA at room temperature with close values of χ^* can be achieved on the surface of both materials by the activation with the Cs_xSb layer in the case of Na₂KSb and the (Cs,O) layer for GaAs.

Third, DFT calculations showed that both semiconductors, Na₂KSb and GaAs, are direct-gap semiconductors with a qualitatively similar band structure [24,53]. Therefore, as in the case of GaAs, the optical orientation of electron spins [12] and emission of spin-polarized electrons into vacuum should take place in MP; recently, this has been experimentally proved by Rusetsky *et al.* [24]. It should be noted that the polycrystallinity of MPs is not an obstacle for the manifestation of the optical orientation since the electronic properties of condensed matter are determined mainly by the short-range order in the atomic structure, which exists within each crystallite. Moreover, replacing the anion, i.e., As in GaAs with Sb in Na₂KSb, leads, as in III-V compounds, to an increase in the spin-orbit splitting of the valence band approximately as Z^2 , where Z is the anion atomic number [78]. This increase facilitates the manifestation of the effect of optical orientation.

The main difference and disadvantage of MPs, compared to III-V semiconductor photocathodes, is the relatively low quantum efficiency values. According to Ref. [28], to a large extent, low QE values are due to the incomplete light absorption in a thin active layer, the thickness of which lies in the range of 100–150 nm and is limited by the small electron diffusion length $L_D \approx 110$ nm. Taking into account that the characteristic crystallite size lies in the range of approximately 10–100 nm [29,69], it is reasonable to assume that both the effective

diffusion length and the active-layer thickness are limited by the crystallite size since the transport of electrons across the boundaries between crystallites is apparently hindered. As a consequence, the MP consists of an array of local photocathodes, each being one separate crystallite. The fluctuations in crystallite sizes in the MP active layer can also contribute to a decrease in QE. A possible way to increase the QE of MPs is to select a substrate and optimize the growth conditions of the active layer in order to increase the crystallite size or to grow MPs epitaxially on a suitable crystalline substrate [59,79].

An advantage of Na₂KSb/Cs_xSb NEA photocathodes, which is revealed in this work, is the possibility to obtain highly directional electron beams, as compared to *p*-GaAs(Cs,O) photocathodes. We believe that this advantage is due to the ordered activation layers that are formed on the MP surfaces, in contrast to the amorphous (Cs,O) layers of III-V semiconductor photocathodes on which photoelectrons are diffusely scattered. A necessary condition for beam directionality is the preferential orientation of the emitting crystallites relative to the photocathode surface. The results of x-ray diffraction and electron-microscopy experiments indicate that this condition is satisfied [58,69].

V. CONCLUSION

In conclusion, we performed the photoemission and optical measurements on Na₂KSb and Na₂KSb/Cs_xSb photocathodes in order to determine their energy-band diagrams and to elucidate the photoemission pathways. The measurements of quantum efficiency, photoluminescence, and absorbance spectra indicated that the Na₂KSb band gap at room temperature is in the range of 1.40–1.44 eV. The measurements of longitudinal energy distribution curves prove that, at room temperature, Na₂KSb photocathodes have positive effective electron affinity of approximately 0.3 eV. The adsorption of Cs and Sb on Na₂KSb leads to a decrease in the effective electron affinity down to negative values and to the reduction in the surface recombination velocity. The effective electron affinity of Na₂KSb/Cs_xSb photocathodes lies in the range from –0.08 to –0.13 eV at room temperature. Upon cooling to the liquid nitrogen temperature, the effective electron affinity of Na₂KSb/Cs_xSb photocathodes further decreases and lies in the range from –0.25 to –0.30 eV.

The comparison of the longitudinal energy-distribution curves of polycrystalline Na₂KSb/Cs_xSb and monocrystalline *p*-GaAs(Cs,O) photocathodes at 80 K reveals the highly directional photoelectron emission from the Na₂KSb/Cs_xSb photocathode, which indicates weak diffuse scattering at its surface, in contrast to the surface of *p*-GaAs(Cs,O). The obtained results open up the opportunities for engineering multialkali NEA photocathodes for

various practical applications, including the development of high-brightness sources of spin-polarized electrons.

ACKNOWLEDGMENTS

The authors acknowledge the support from the Russian Science Foundation (Grant No. 22-12-20024, p-9), SRF SKIF Boreskov Institute of Catalysis (FWUR-2024-0042) and ISP SB RAS.

- [1] A. Accardi *et al.*, Electron-Ion Collider: The next QCD frontier, *Eur. Phys. J. A* **52**, 268 (2016).
- [2] D. Becker *et al.*, The P2 experiment, *Eur. Phys. J. A* **54**, 208 (2018).
- [3] D. P. Anderle *et al.*, Electron-ion collider in China, *Front. Phys.* **16**, 64701 (2021).
- [4] E. Sickling and R. Ström, From precision physics to the energy frontier with the Compact Linear Collider, *Nat. Phys.* **16**, 386 (2020).
- [5] H. Yamamoto, The International Linear Collider Project—Its Physics and Status, *Symmetry* **13**, 674 (2021).
- [6] M. N. Achasov, V. E. Blinov, A. V. Bobrov, D. A. Bodrov, A. E. Bondar', V. S. Vorobiev, D. S. Gorbunov, V. P. Druzhinin, D. A. Epifanov, A. S. Kuzmin, I. B. Logashenko, D. V. Matvienko, A. V. Nefediev, P. N. Pakhlov, G. V. Pakhlova, V. E. Popov, and T. V. Uglov, Experiments at the Super Charm-Tau factory, *Physics-Uspekhi* **67**, 55 (2024).
- [7] M. Kuwahara, S. Kusunoki, X. G. Jin, T. Nakanishi, Y. Takeda, K. Saitoh, T. Ujihara, H. Asano, and N. Tanaka, 30-kV spin-polarized transmission electron microscope with GaAs–GaAsP strained superlattice photocathode, *Appl. Phys. Lett.* **101**, 033102 (2012).
- [8] L. Yu, W. Wan, T. Koshikawa, M. Li, X. Yang, C. Zheng, M. Suzuki, T. Yasue, X. Jin, Y. Takeda, R. Tromp, and W.-X. Tang, Aberration corrected spin polarized low energy electron microscope, *Ultramicroscopy* **216**, 113017 (2020).
- [9] R. L. Bell, *Negative Electron Affinity Devices* (Clarendon Press, Oxford, 1973).
- [10] O. H. W. Siegmund, A. S. Tremsin, and J. V. Vallerga, Advanced MCP sensors for UV/visible astronomy and biology, *Nucl. Instrum. Meth. A* **510**, 185 (2003).
- [11] S. Uchiyama, Y. Takagi, M. Niigaki, H. Kan, and H. Kondoh, GaN-based photocathodes with extremely high quantum efficiency, *Appl. Phys. Lett.* **86**, 103511 (2005).
- [12] *Optical orientation*, edited by F. Meier and B. P. Zakharchenya (North-Holland, Amsterdam, 1984).
- [13] D. T. Pierce, F. Meier, and P. Zürcher, Negative electron affinity GaAs: A new source of spinpolarized electrons, *Appl. Phys. Lett.* **86**, 670 (1975).
- [14] H.-J. Drouhin, C. Hermann, and G. Lampel, Photoemission from activated gallium arsenide. II. Spin polarization versus kinetic energy analysis, *Phys. Rev. B* **31**, 3872 (1985).
- [15] W. Liu, Y. Chen, W. Lu, A. Moy, M. Poelker, M. Stutzman, and S. Zhang, Record-level quantum efficiency from a high polarization strained GaAs/GaAsP superlattice photocathode with distributed Bragg reflector, *Appl. Phys. Lett.* **109**, 252104 (2016).

- [16] A. H. Sommer, New photoemissive cathodes of high sensitivity, *Rev. Sci. Instrum.* **26**, 725 (1955).
- [17] W. E. Spicer, Photoemissive, photoconductive, and optical absorption studies of alkali-antimony compounds, *Phys. Rev.* **112**, 114 (1958).
- [18] B. Erjavec, Growth and stoichiometry of the Cs_xSb surface film of a high-efficiency, multialkali-antimonide photocathode, *Thin Solid Films* **303**, 4 (1997).
- [19] P. Dolizy, Growth of alkali-antimonide films for photocathodes, Philips Tech. Rev. **40**, 19 (1982).
- [20] V. S. Rusetsky, V. A. Golyashov, A. V. Mironov, A. Y. Demin, and O. E. Tereshchenko, Photoemission properties of a multialkali photocathode, *Optoelectron. Instrum. Data Process.* **57**, 505 (2021).
- [21] B. Dunham *et al.*, Record high-average current from a high-brightness photoinjector, *Appl. Phys. Lett.* **102**, 034105 (2013).
- [22] L. Cultrera, C. Gulliford, A. Bartnik, H. Lee, and I. Bazarov, Ultra low emittance electron beams from multialkali antimonide photocathode operated with infrared light, *Appl. Phys. Lett.* **108**, 134105 (2016).
- [23] P. Musumeci, J. G. Navarro, J. B. Rosenzweig, L. Cultrera, I. Bazarov, J. Maxson, S. Karkare, and H. Padmore, Advances in bright electron sources, *Nucl. Instrum. Meth. A* **907**, 209 (2018).
- [24] V. S. Rusetsky, V. A. Golyashov, S. V. Eremeev, D. A. Kustov, I. P. Rusinov, T. S. Shamirzaev, A. V. Mironov, A. Y. Demin, and O. E. Tereshchenko, New spin-polarized electron source based on alkali antimonide photocathode, *Phys. Rev. Lett.* **129**, 166802 (2022).
- [25] H.-J. Drouhin, C. Hermann, and G. Lampel, Photoemission from activated gallium arsenide. I. Very-high-resolution energy distribution curves, *Phys. Rev. B* **31**, 3859 (1985).
- [26] C. Ghosh and B. P. Varma, Preparation and study of properties of a few alkali antimonide photocathodes, *J. Appl. Phys.* **49**, 4549 (1978).
- [27] E.-L. Hoene, Optical and photoelectric properties of multialkali photocathodes, *Adv. Electron. Electron Phys.* **33**, 369 (1972).
- [28] V. P. Beguchev, I. A. Shefova, and A. L. Musatov, Optical and photoemissive properties of multi-alkali photocathodes, *J. Phys. D: Appl. Phys.* **26**, 1499 (1993).
- [29] W. H. McCarroll, R. J. Paff, and A. H. Sommer, Role of Cs in the $(\text{Cs})\text{Na}_2\text{KSb}$ (S-20) multialkali photocathode, *J. Appl. Phys.* **42**, 569 (1971).
- [30] R. Holtom, G. P. Hopkins, and P. M. Gundry, Surface studies of multialkali antimonide (S20/S25) photocathodes, *J. Appl. Phys.* **12**, 1169 (1979).
- [31] G. E. Pikus and A. N. Titkov, in *Optical orientation*, edited by F. Meier and B. P. Zakharchenya (North-Holland, Amsterdam, 1984), p. 73..
- [32] P. H. Song and K. W. Kim, Spin relaxation of conduction electrons in bulk III-V semiconductors, *Phys. Rev. B* **66**, 035207 (2002).
- [33] D. A. Orlov, V. E. Andreev, and A. S. Terekhov, Elastic and inelastic tunneling of photoelectrons from the dimensional quantization band at a p^+ -GaAs-(Cs, O) interface into vacuum, *JETP Lett.* **71**, 151 (2000).
- [34] V. V. Bakin, A. A. Pakhnevich, S. N. Kosolobov, H. E. Scheibler, A. S. Jaroshevich, and A. S. Terekhov, Refraction of thermalized electrons emitted ballistically into vacuum from p^+ -GaAs-(Cs, O), *JETP Lett.* **77**, 167 (2003).
- [35] A. A. Rodionov, V. A. Golyashov, I. B. Chistokhin, A. S. Jaroshevich, I. A. Derebezov, V. A. Haisler, T. S. Shamirzaev, I. I. Marakhovka, A. V. Kopotilov, N. V. Kislykh, A. V. Mironov, V. V. Aksenov, and O. E. Tereshchenko, Photoemission and injection properties of a vacuum photodiode with two negative-electron-affinity semiconductor electrodes, *Phys. Rev. Appl.* **8**, 034026 (2017).
- [36] S. Pastuszka, D. Kratzmann, D. Schwalm, A. Wolf, and A. S. Terekhov, Transverse energy spread of photoelectrons emitted from GaAs photocathodes with negative electron affinity, *Appl. Phys. Lett.* **71**, 2967 (1997).
- [37] L. Cultrera, S. Karkare, H. Lee, X. Liu, I. Bazarov, and B. Dunham, Cold electron beams from cryocooled, alkali antimonide photocathodes, *Phys. Rev. ST Accel. Beams* **18**, 113401 (2015).
- [38] O. E. Tereshchenko, V. A. Golyashov, V. S. Rusetsky, D. A. Kustov, A. V. Mironov, and A. Y. Demin, Vacuum spin LED: First step towards vacuum semiconductor spintronics, *Nanomaterials* **13**, 422 (2023).
- [39] O. E. Tereshchenko, V. A. Golyashov, A. A. Rodionov, I. B. Chistokhin, N. V. Kislykh, A. V. Mironov, and V. V. Aksenov, Solar energy converters based on multi-junction photoemission solar cells, *Sci. Rep.* **7**, 16154 (2017).
- [40] V. L. Alperovich, Y. B. Bolkhovityanov, A. S. Jaroshevich, A. V. Katkov, M. A. Revenko, H. E. Scheibler, and A. S. Terekhov, Shifts and splitting of energy bands in elastically strained InGaP/GaAs(111)B epitaxial films, *J. Appl. Phys.* **82**, 1214 (1997).
- [41] J. W. Schwede, T. Sarmiento, V. K. Narasimhan, S. J. Rosenthal, D. C. Riley, F. Schmitt, I. Bargatin, K. Sahasrabudde, R. T. Howe, J. S. Harris, N. A. Melosh, and Z.-X. Shen, Photon-enhanced thermionic emission from heterostructures with low interface recombination, *Nat. Commun.* **4**, 1576 (2013).
- [42] A. G. Zhuravlev, A. S. Romanov, and V. L. Alperovich, Photon-enhanced thermionic emission from p -GaAs with nonequilibrium Cs overlayers, *Appl. Phys. Lett.* **105**, 251602 (2014).
- [43] A. S. Terekhov and D. A. Orlov, Fine structure in the spectra of thermalized photoelectrons emitted from GaAs with negative electron affinity, *JETP Lett.* **59**, 864 (1994).
- [44] S. R. Johnson and T. Tiedje, Temperature dependence of the Urbach edge in GaAs, *J. Appl. Phys.* **78**, 5609 (1995).
- [45] J. B. Cui, J. Ristein, and L. Ley, Low-threshold electron emission from diamond, *Phys. Rev. B* **60**, 16135 (1999).
- [46] A. A. Pakhnevich, V. V. Bakin, A. V. Yaz'kov, H. E. Scheibler, S. V. Shevelev, O. E. Tereshchenko, A. S. Yaroshevich, and A. S. Terekhov, Energy distributions of photoelectrons emitted from p -GaN(Cs, O) with effective negative electron affinity, *JETP Lett.* **79**, 479 (2004).
- [47] A. A. Pakhnevich, V. V. Bakin, H. E. Scheibler, and A. S. Terekhov, Emission of ballistic photoelectrons from p -GaN(Cs, O) with the effective negative electron affinity, *Phys. Solid State* **49**, 2070 (2007).

- [48] A. A. Dowman, T. H. Jones, and A. H. Beck, Scanning electron diffraction studies on alkali antimonide photocathodes, including the S20, *J. Phys. D: Appl. Phys.* **8**, 69 (1975).
- [49] L. Galan and C. W. Bates, Jr., Structure of multialkali antimonide photocathodes studied by x-ray photoelectron spectroscopy, *J. Phys. D: Appl. Phys.* **14**, 293 (1981).
- [50] M. Piccardo, L. Martinelli, J. Iveland, N. Young, S. P. DenBaars, S. Nakamura, J. S. Speck, C. Weisbuch, and J. Peretti, Determination of the first satellite valley energy in the conduction band of wurtzite GaN by near-band-gap photoemission spectroscopy, *Phys. Rev. B* **89**, 235124 (2014).
- [51] I. Vurgaftman, J. R. Meyer, and L. R. Ram-Mohan, Band parameters for III–V compound semiconductors and their alloys, *J. Appl. Phys.* **89**, 5815 (2001).
- [52] A. P. Levanyuk and V. V. Osipov, Edge luminescence of direct-gap semiconductors, *Sov. Phys. Usp.* **24**, 187 (1981).
- [53] R. Amador, H.-D. Saßnick, and C. Cocchi, Electronic structure and optical properties of Na₂KSb and NaK₂Sb from first-principles many-body theory, *J. Phys.: Condens. Matter* **33**, 365502 (2021).
- [54] W. McCarroll, Phases in the photoelectric sodium-potassium antimony system, *J. Phys. Chem. Solids* **16**, 30 (1960).
- [55] A. R. H. F. Ettema and R. A. de Groot, Electronic structure of Na₃Sb and Na₂KSb, *Phys. Rev. B* **61**, 10035 (2000).
- [56] C. H. Qiu and J. I. Pankove, Deep levels and persistent photoconductivity in GaN thin films, *Appl. Phys. Lett.* **70**, 1983 (1997).
- [57] M. Brinza, J. Willekens, M. L. Benkhedir, E. V. Emelianova, and G. J. Adriaenssens, Photoconductivity methods in materials research, *J. Mater. Sci. Mater. Electron.* **16**, 703 (2005).
- [58] P. Dolizy, F. Grolière, and M. Lemonier, High performance with trialkaline antimonide photocathodes, *Adv. Electron. Electron Phys.* **74**, 331 (1988).
- [59] C. T. Parzyck, C. A. Pennington, W. J. I. DeBenedetti, J. Balajka, E. M. Echeverria, H. Paik, L. Moreschini, B. D. Faeth, C. Hu, J. K. Nangoi, V. Anil, T. A. Arias, M. A. Hines, D. G. Schlom, A. Galdi, K. M. Shen, and J. M. Maxson, Atomically smooth films of CsSb: A chemically robust visible light photocathode, *APL Mater.* **11**, 101125 (2023).
- [60] D. G. Fisher, A. F. McDonie, and A. Sommer, Band-bending effects in Na₂KSb and K₂CsSb photocathodes, *J. Appl. Phys.* **45**, 487 (1974).
- [61] W. E. Spicer, Z. Liliental-Weber, E. Weber, T. K. N. Newman, R. Cao, C. McCants, P. Mahowald, K. Miyano, and I. Lindau, The advanced unified defect model for Schottky barrier formation, *J. Vac. Sci. Tech. B* **6**, 1245 (1988).
- [62] D. A. Orlov, M. Hoppe, U. Weigel, D. Schwalm, A. S. Terekhov, and A. Wolf, Energy distributions of electrons emitted from GaAs(Cs,O), *Appl. Phys. Lett.* **78**, 2721 (2001).
- [63] D. C. Rodway and M. B. Allenson, In situ surface study of the activating layer on GaAs(Cs,O) photocathodes, *J. Phys. D: Appl. Phys.* **19**, 1353 (1986).
- [64] V. V. Bakin, K. V. Toropetsky, H. E. Scheibler, A. S. Terekhov, L. B. Jones, B. L. Milityn, and T. C. Q. Noakes, *p*-GaAs(Cs, O)-photocathodes: Demarcation of domains of validity for practical models of the activation layer, *Appl. Phys. Lett.* **106**, 183501 (2015).
- [65] B. Goldstein, LEED-Auger characterization of GaAs during activation to negative electron affinity by the adsorption of Cs and O, *Surf. Sci.* **47**, 143 (1975).
- [66] J. Kim, M. C. Gallagher, and R. F. Willis, Cs adsorption on *n*- and *p*-type GaAs(001)(2 × 4) surfaces, *Appl. Surf. Sci.* **67**, 286 (1993).
- [67] M. Hirao, D. Yamanaka, T. Yazaki, J. Osako, H. Iijima, T. Shiokawa, H. Akimoto, and T. Meguro, STM study on adsorption structures of Cs on the As-terminated GaAs(001)(2 × 4) surface by alternating supply of Cs and O₂, *IEICE Trans. Electron.* **E99-C**, 376 (2016).
- [68] S. Gemming, G. Seifert, C. Mühle, M. Jansen, A. Albu-Yaron, T. Arad, and R. Tenne, Electron microscopy, spectroscopy, and first-principles calculations of Cs₂O, *J. Solid State Chem.* **178**, 1190 (2005).
- [69] T. Ninomiya, K. Taketoshi, and H. Tachiya, Crystal structure of multialkali photocathodes, *Adv. Electron. Electron Phys.* **28**, 337 (1969).
- [70] S. Luryi and E. Suhir, New approach to the high quality epitaxial growth of lattice-mismatched materials, *Appl. Phys. Lett.* **49**, 140 (1986).
- [71] L. B. Jones, H. E. Scheibler, D. V. Gorshkov, A. S. Terekhov, B. L. Milityn, and T. C. Q. Noakes, Evolution of the transverse and longitudinal energy distributions of electrons emitted from a GaAsP photocathode as a function of its degradation state, *J. Appl. Phys.* **121**, 225703 (2017).
- [72] V. L. Alperovich, A. G. Paulish, and A. S. Terekhov, Domination of adatom-induced over defect-induced surface states on *p*-type GaAs(Cs,O) at room temperature, *Phys. Rev. B* **50**, 5480 (1994).
- [73] V. S. Khoroshilov, D. M. Kazantsev, S. A. Rozhkov, and V. L. Alperovich, Surface photovoltage in heavily doped *p*⁺-GaAs with adsorbed cesium and oxygen overlayers, *Tech. Phys. Lett.* **49**, 21 (2023).
- [74] A. D. Korinfskii and A. L. Musatov, Effect of surface recombination on photoelectric emission from semiconductors with a negative electron affinity, *JETP Lett.* **37**, 547 (1983).
- [75] T. Kuhn and G. Mahler, Surface models for perpendicular ambipolar transport in kinetic and hydrodynamic theories, *Phys. Rev. B* **40**, 12147 (1989).
- [76] R. J. Nelson and R. G. Sober, Minority-carrier lifetimes and internal quantum efficiency of surface-free GaAs, *J. Appl. Phys.* **49**, 6103 (1978).
- [77] D. Garbuzov, The efficiency and radiative lifetime concentration dependences for the direct band-gap GaAs-like semiconductors, *Czech. J Phys. B* **30**, 326 (1980).
- [78] P. Carrier and S.-H. Wei, Calculated spin-orbit splitting of all diamondlike and zinc-blende semiconductors: Effects of *p*_{1/2} local orbitals and chemical trends, *Phys. Rev. B* **70**, 035212 (2004).
- [79] C. T. Parzyck, A. Galdi, J. K. Nangoi, W. J. I. DeBenedetti, J. Balajka, B. D. Faeth, H. Paik, C. Hu, T. A. Arias, M. A. Hines, D. G. Schlom, K. M. Shen, and J. M. Maxson, Single-crystal alkali antimonide photocathodes: High efficiency in the ultra-thin limit, *Phys. Rev. Lett.* **128**, 114801 (2022).